Rapid Communications

Phase-matched optical second harmonic generation in a hyperbolic metamaterial based on silver nanorods

I. A. Kolmychek,[1,*] I. V. Malysheva,[1] V. B. Novikov,[1] A. P. Leontiev,[2] K. S. Napolskii,[2,3] and T. V. Murzina[1]

[1]*Department of Physics, Moscow State University, 119991 Moscow, Russia*

[2]*Department of Materials Science, Moscow State University, 119991 Moscow, Russia*

[3]*Department of Chemistry, Moscow State University, 119991 Moscow, Russia*

(Received 15 September 2020; revised 12 November 2020; accepted 24 November 2020; published 11 December 2020)

Artificial hyperbolic metamaterials (HMM) are perspective for the nonlinear optical applications, their exciting functionality being due to the hyperbolic dispersion induced by a strong shape anisotropy. Here we study the second harmonic generation (SHG) in HMM formed by arrays of silver nanorods in anodic alumina. In the hyperbolic dispersion regime, giant SHG is observed associated with the fulfillment of the phase-matching conditions supported by the epsilon-near-pole resonance at the SHG wavelength, and an increase in the pump field in the epsilon-near-zero (ENZ) spectral range. We predict a strong increase in the SHG efficiency for metamaterials with the ENZ resonance at the second harmonic frequency.

DOI: 10.1103/PhysRevB.102.241405

Hyperbolic metamaterials (HMM) received much interest recently owing to their unique optical and nonlinear optical properties originating from artificial hyperbolic dispersion instead of elliptical one intrinsic to traditional media [1,2]. HMM are artificial metal-dielectric nanocomposites with a uniaxial anisotropy and opposite in sign principle components of the optical permittivity and/or permeability [3–6]. In the case of nonmagnetic HMMs ($\mu = 1$) characterized by the principle components of its dielectric tensor $\varepsilon_{\parallel} \cdot \varepsilon_{\perp} < 0$, the isofrequency surface for the TM mode of light is the hyperbolic function

$$\frac{q_x^2 + q_y^2}{\varepsilon_{\parallel}} + \frac{q_z^2}{\varepsilon_{\perp}} = \left(\frac{\omega}{c}\right)^2, \tag{1}$$

where ω is the frequency of the electromagnetic wave, $q_{x,y,z}$ are the wave vector components, c is the speed of light, the optical axis is along the z axis. The simplest HMM designs are metal-dielectric multilayered films, or ordered arrays of metallic nanorods in a dielectric matrix. In both cases, the spectra of the HMM effective $\hat{\varepsilon}$ components reveal two specific features. The first one is the sign reversal of the real part of $\varepsilon_{\parallel}$ or $\varepsilon_{\perp}$, i.e. passing it through zero value (epsilon-near-zero, ENZ). The second is the pole of the effective dielectric constant (epsilon-near-pole, ENP) [7]. These HMM features are responsible for a number of perspective phenomena such as negative refraction [8], giant birefringence [9,10], resonant enhancement of the optical response [11–13].

Hyperbolic metamaterials are as well a viable platform for a manyfold increase in nonlinear-optical effects. Indeed, a substantial increase in the electric field of light was observed inside the metal-nanorod based HMM close to the ENZ spectral point [14]. This almost singular growth of the optical field led to the enhancement of a number of nonlinear-optical effects including second [15–18] and third harmonics generation [19,20] and self-action of light [21]. As compared to isotropic natural ENZ media (such as CaF_2, TiN, ITO, SiC, etc.) [22], an important advantage of composite HMM is that their dispersion and ENZ spectral position can be controlled by a proper choice of the geometrical parameters [23]. This allows for the fulfillment of the phase-matching conditions as has been predicted for the case of sum and difference harmonics generation [24–26]. At the same time, the second-order nonlinear-optical effects that involve both types of HMM critical points, ENP and ENZ, have not been discussed up to now.

In this Rapid Communication, we describe giant optical second harmonic generation (SHG) in composite silver nanorods/porous anodic alumina HMM designed in such a way that both critical points, ENZ (at the fundamental wavelength) and ENP (at the SHG one), are involved in the nonlinear interaction. Our main finding consists in a drastic increase in the SHG signal in a narrow spectral interval close to the two-photon ENP resonance. According to our modeling, this is due to the realization of the SHG phase-matching caused by the hyperbolic dispersion of the composite at the fundamental wavelength and further SHG increase induced by the two-photon ENP resonance. We predict also dramatic increase in the SHG efficiency when the wavelength of the nonlinear response corresponds to the ENZ point owing to the resonant enhancement of the Purcell factor inside the HMM.

Arrays of silver nanorods were prepared by templated electrodeposition of Ag inside the pores of anodic aluminum oxide (AAO). SEM image [Fig. 1(a)] proved that the diameter and the distance between the centers of neighboring nanorods coincide with the pore diameter (41 ± 9 nm) and interpore distance (105 ± 14 nm) in AAO, respectively. Thus the volume fraction of silver in the filled part of the template coincides with the template porosity of about 14%. According to

*irisha@shg.ru

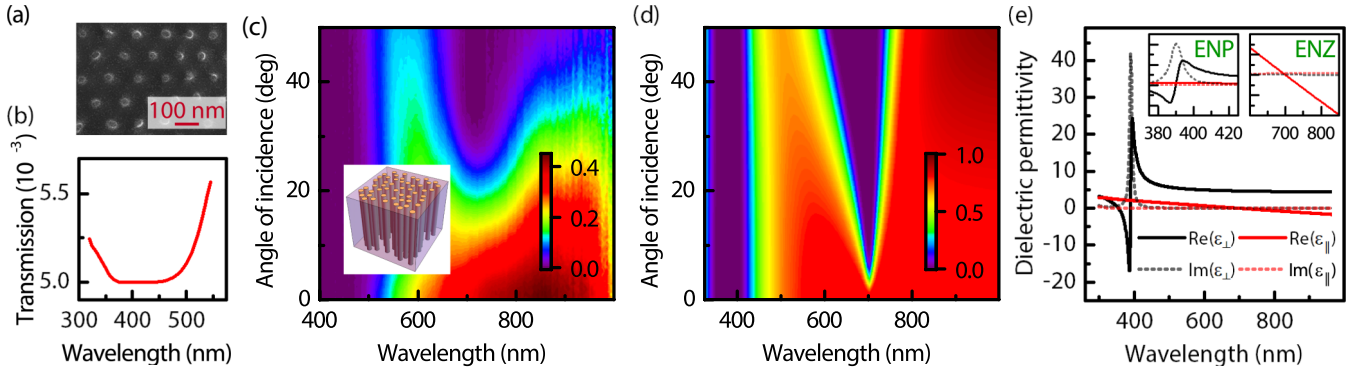

FIG. 1. (a) SEM image of the bottom side of Ag/AAO nanocomposite. (b) Transmission spectrum of the HMM structure in short wavelength region at normal incidence. (c), (d) Experimental and calculated angular-wavelength transmission spectra of HMM for *p*-polarized light. Inset is sketch of the HMM structure. (e) Calculated spectra of the effective permittivity tensor components of HMM.

cross-sectional SEM image of the nanocomposite, the length of the nanorods was 430 ± 160 nm.

Figure 1(c) shows the HMM angular-wavelength transmission spectrum measured for the *p*-polarized incident radiation using a home-made setup based on a halogen lamp as a broadband light source. At oblique incidence, it demonstrates two minima centered at 710 and 420 nm; the latter was estimated from the measurements of transmission performed by the commercial "Lomo-spectr SF-56" spectrophotometer at normal incidence, as it allows one to study the UV part of the spectra [Fig. 1(b)]. Minima in Fig. 1(c) correspond to increased light absorption in the spectral vicinity of the pole (at 420 nm) and zero (at 710 nm) of the HMM permittivity components, similarly to observed recently for Au-nanorods based composite [27]. The spectra of the ordinary ($\varepsilon_\perp$) and extraordinary ($\varepsilon_\parallel$) components of the HMM dielectric permittivity, calculated within the effective medium approximation [28] for the composite HMM under study, reveal a pole of $\varepsilon_\perp$ at the wavelength $\lambda \approx 390$ nm and $\varepsilon_\parallel = 0$ at $\lambda \approx 700$ nm (ENZ), the dielectric constants of Ag and alumina were taken from Refs. [29,30]. These wavelengths correspond well to the experimental transmission spectrum [Figs. 1(b) and 1(c)] for the porosity of the HMM of about 16% and for the averaged parameters of nanorods. The effective medium model used for the calculations treats the HMM in the local field approximation, nevertheless it reproduces well the main peculiarities of the optical response of HMMs and is successive in modeling similar nanostructures [9]. The hyperbolic dispersion regime of our HMM was realized in the wavelength region $\lambda > 700$ nm at oblique incidence of *p*-polarized light. At the same time, at normal incidence or for the *s*-polarized fundamental beam only the short-wavelength ENP resonance was excited and the relevant transmission minimum remained pronounced.

Angular-wavelength transmission spectra of the effective HMM layer with the parameters identical to the experimental ones were calculated by the transfer-matrix method adapted for the anisotropic media [Fig. 1(d)]. In our numerical method, we switch off the multiple interference of light in the HMM slab to eliminate spurious oscillations of light intensity that are absent in the experimental linear transmission spectrum shown in Fig. 1(c), which is probably due to the variation of the length of metal nanorods in the HMM. In calculated spectra transmission minima of the *p*-polarized light at 390-nm and 700-nm wavelengths appear associated with the ENP and ENZ points, respectively [Fig. 1(d)]. One can see a good correlation between the experimental and simulation results shown in Figs. 1(c) and 1(d). Deviations of the experimental value of the ENP wavelength from the simulated one can be due to the limitations of the effective medium approach and of the Ag nanorods' permittivity from that of the bulk material taken for the simulations.

For the experimental studies of the second harmonic generation in HMM, we used the radiation of a femtosecond Ti:Sa laser with the wavelength tunable from 750 to 900 nm, FWHM of the spectral line of about $\Delta\lambda = 5$–10 nm, the pulse duration of 50 fs, the repetition rate of 80 MHz, and the average power of 50 mW. The pump beam was focused on the HMM film into a spot of 50 μm in diameter. The transmitted *p*-polarized SHG radiation was spectrally selected by color filters and detected by a photomultiplier operating in the photon-counting mode. The intensity of the *s*-polarized SHG was absent within the experimental accuracy, as expected for the in-plane isotropic nonlinear media [31]. We suppose that effect of the nonlinear refraction in the HMM under the applied femtosecond radiation does not appear in our SHG experiments. It stems from the large spectral width of laser pulse $\Delta\lambda$ compared to expected spectral shift $\delta\lambda$ of the ENZ resonance under illumination of the HMM, which is estimated as $\delta\lambda = 0.3$ nm for the considered light intensity and the nonlinear refractive index of the typical ENZ material (indium-tin-oxide), which possesses $n_2 \approx 10^{-15}$ m^2/W [14].

Figures 2(a) and 2(b) show the measured normalized angular-wavelength spectra of the transmitted SHG intensity $I_{2\omega}$, measured for the *p* and *s* polarizations of the fundamental beam. In the case of the *p* polarization, the highest SHG intensity was attained at the edges of the available spectral range for oblique angles of incidence of 20°–30°, where the SHG intensity was approximately 30 times higher than in the off-resonant conditions. For the *s*-polarized laser beam [Fig. 2(b)] the overall SHG intensity was much lower as compared to the *p*-polarized one, while also revealed a maximum at long wavelengths [Fig. 2(b)].

For numerical simulations of the SHG process we solved the Maxwell equations with the nonlinear polarization source

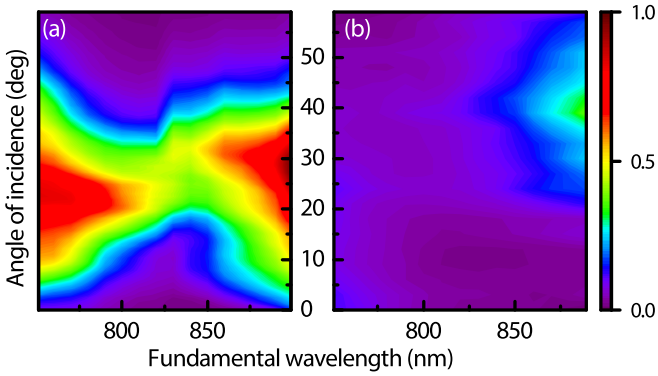

FIG. 2. Experimental angular-wavelength intensity spectra of the *p*-polarized component of SH radiation generated in HMM slab in transmitted direction by (a) *p*- and (b) *s*-polarized pump.

term using the developed nonlinear transfer-matrix method within the undepleted-pump approximation. The calculation of distributions of the second harmonic (SH) field in the HMM and of the outgoing SHG power was performed in two steps. First, the linear problem of the fundamental light transmission through the HMM slab was solved by the linear transfer-matrix method, giving the spatial dependence of fundamental field and consequent vectorial nonlinear polarization distribution. At the second step, this SHG polarization served as the source term in inhomogeneous Maxwell equations that were solved for the estimation of the outgoing. We took care of a strong anisotropy of the HMM permittivity and second-order susceptibility $\hat{\chi}^{(2)}$ tensors.

In the simulations, we used the coordinate frame with the Oz axis parallel to the HMM optical axis (i.e., along the nanorods), Ox and Oy axes lying in the HMM interface. We assumed that the nonzero $\hat{\chi}^{(2)}$ components of the HMM are $\chi^{(2)}_{zzz}$, $\chi^{(2)}_{zxx}$, and $\chi^{(2)}_{zyy}$ that gives *p*-polarized second harmonic signal for both *p* and *s* cases of the fundamental field polarization, as was observed in the experiments [Figs. 2(a) and 2(b)]. These nonzero components of $\hat{\chi}^{(2)}$ correspond to the in-plane isotropy of HMM and ensure the absence of SHG at normal incidence of light, in agreement with the experimental results [Figs. 2(a) and 2(b)].

Figures 3(a) and 3(b) show the calculated spectra of the SHG intensity transmitted through the HMM for *p*- and *s*-polarized fundamental beams in a wide spectral range. For the convenience of comparison of the experimental and theoretical results, these numerical results in a narrower spectral range that corresponds to the experimental graphs are shown in Figs 3(c) and 3(d). For the *p* polarization, a number of SHG maxima appear that can be divided into two groups. The first group includes two SHG maxima at (i) $\lambda \lesssim 700$ nm, i.e., in the spectral vicinity of the ENZ point and for the angle of incidence $\theta = 20°$–$30°$, and (ii) the SHG maximum at $\lambda = 820$ nm at $\theta \approx 50°$–$60°$ [Fig. 3(c)]. Second group of the SH maxima is close to the fundamental wavelength $\lambda = 2\lambda_{\mathrm{ENZ}}$, i.e., near 1400 nm [Figs. 3(a) and 3(b)]. According to our analysis, all these SHG spectral peaks are nothing but the result of the fulfillment of the type-0 (*eee*) phase-matching condition in a uniaxial HMM, as the extraordinary SHG wave is generated by the extraordinary fundamental one. This is

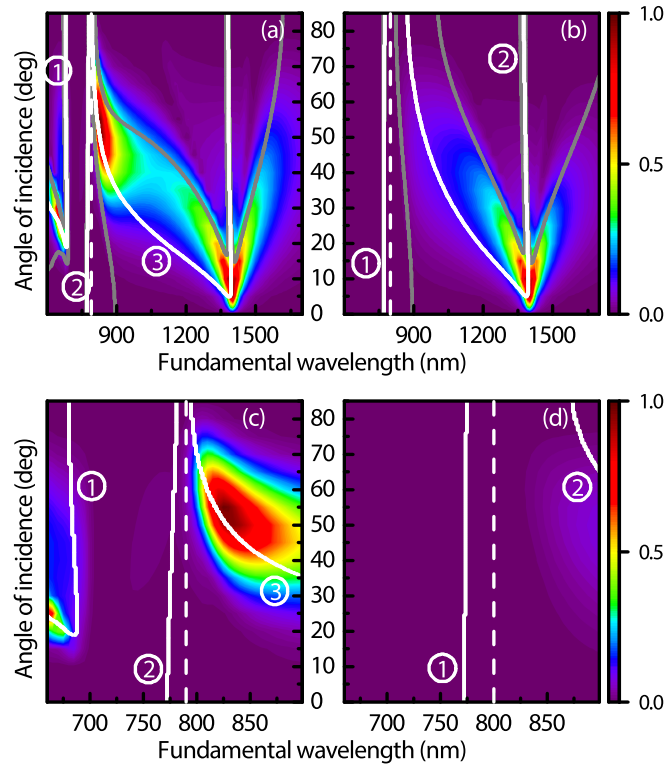

FIG. 3. Calculated angular-wavelength intensity spectra of the *p*-polarized SH radiation generated in transmission through the HMM slab by (a) *p*- and (b) *s*-polarized pump. [(c) and (d)] The same spectra in smaller spectral range. Dashed lines: fundamental wavelengths that generate the second harmonic at the ENP wavelength; solid white curves labeled by numbers correspond to different types of the SHG phase-matching conditions; grey ones correspond to phase-mismatch when $L_c(\lambda, \theta) = L_{\mathrm{HMM}}$.

illustrated in Fig. 3(a), where the wavelength-angular spectra of the *eee* phase-matching conditions are shown by three solid white curves. These contours were obtained by solution of the equation

$$2q_z(\lambda, \theta) = q_z(\lambda/2, \theta), \tag{2}$$

where q_z satisfies Eq. (1).

We would like to stress that the SHG enhancement due to the phase-matching requires the combination of resonant behavior of the HMM refractive index at both the ENZ and ENP wavelengths. Indeed, the studied HMM exhibits the hyperbolic dispersion for *p*-polarized light at $\lambda > \lambda_{\mathrm{ENZ}}$, where the propagation constant of light inside the metamaterial, q_z, is large and varies resonantly near λ_{ENZ}. This is illustrated by the angular-wavelength dependence $q_z(\lambda, \theta)$ normalized by the vacuum wave number k_0 for the extraordinary fundamental and SH waves (red surface in Fig. 4). One can see that in the case of the *p*-polarized fundamental light the HMM effective refractive index of (q_z/k_0) routinely achieves the value of eight in the hyperbolic regime ($\lambda >$ 700 nm), which is an unprecedentedly high for natural media. On the other hand, large HMM refractive index at the SHG wavelength is caused by the pole of $\varepsilon_\perp$ [Fig. 1(e)]. The resonant growth of q_z/k_0 at the two-photon ENP wavelength is shown by the blue surface in Fig. 4. As the result,

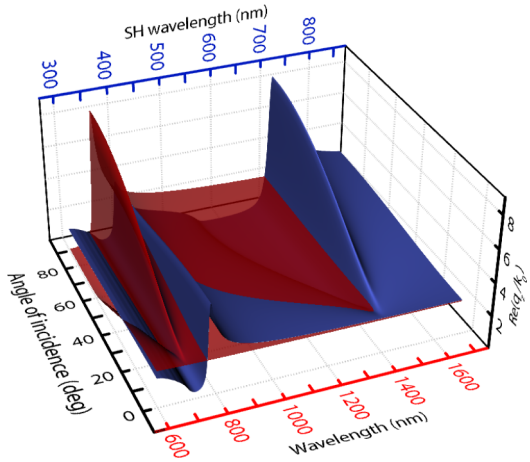

FIG. 4. Angular-wavelength dependencies of propagation constants normalized to vacuum wave number for *p*-polarized fundamental (red surface) and second harmonic (blue surface) radiations in the HMM.

the *eee* phase-matching conditions are realized along several intersections of both surfaces (at the fundamental and second harmonic spectral ranges) and provide the SHG spectral maxima [see Fig. 3(a)]. Intersections exactly correspond to white curves in Fig. 3(a). Similar white curves shown in Fig. 3(b) correspond to type-I (*ooe*) phase-matching conditions, when *p*-polarized SH wave is generated in the HMM by *s*-polarized laser radiation. In this case the contours were obtained by solving Eq. 2 when $\varepsilon_{\parallel}$ for fundamental radiation is replaced by $\varepsilon_{\perp}$ in Eq. (1).

The role of the phase-matching conditions in the appearance of the short-wavelength SHG maximum at $\lambda < 700$ nm is confirmed by its specific two-lobe shape [Fig. 3(a)], which follows precisely the bending of the phase-matching spectral curve (denoted as *1*) near the ENZ wavelength of the HMM. Moreover, at this same wavelength, an enhancement of the normal component of the fundamental electric field takes place [32,33]. The combination of the two effects, i.e., the SHG phase-matching and the resonant growth of the pump field, results in the observed strong SHG increase.

The second branch of the SHG phase-matching conditions (labeled by *2*) that is almost independent on the angle of incidence, is attained at the fundamental wavelength near 780 nm [Fig. 3(a)] when the SHG wavelength corresponds to the ENP spectral range. This branch does not lead to the SHG increase due of extremely high optical losses for SH radiation in this spectral range, where the imaginary part of $\varepsilon_{\perp}$ reveals a maximum [dashed curve in Fig. 1(e)].

The SHG phase-matching condition (curve *3*) leads to the appearance of another SHG maximum at $\lambda \approx 820$ nm and 50°–60° angle of incidence [Fig. 3(a)].

The second group of the SHG maxima near 1400 nm that appears for the *p*-polarized fundamental beam corresponds to the case when the SHG wavelength is close to the ENZ point, i.e., the pump wavelength is $\lambda = 2\lambda_{\mathrm{ENZ}}$ [Fig. 3(a)]. We attribute this effect to the resonant enhancement of the Purcell factor for the nonlinear dipoles oscillating in z direction for the wavelengths close to that of the ENZ point. The increase in the Purcell factor stems from (i) the Lorentz reciprocity theorem [34] and (ii) manyfold increase in the z component of the electric field of light of the wavelength λ_{ENZ} inside the HMM slab. We demonstrate that the SHG maxima have specific V-like shape at inclined light incidence, as shown in Fig. 3(a). It originates from just mentioned enhanced SH emission by z-oriented nonlinear dipoles, that contribute to the SHG only at oblique incidence of the pump wave. Besides in the spectral vicinity of the ENZ wavelength it is affected by the SHG attenuation, which increases with the angle of incidence and leads to the appearance of the SHG minimum in the central part of V-like maximum in Fig. 3(a). Finally, the fulfillment of the *eee* phase-matching condition shown by the white curve labeled by 3 in Fig 3(a) can intensify the SHG signal. In contrast to the case of *p*-polarized laser beam, we observed solely a single V-like SHG maximum in the angular-wavelength map for the *s* polarization of the fundamental beam with the wavelength near $2\lambda_{\mathrm{ENZ}}$ [Fig. 3(b)]. Again, it originates from (i) the Purcell factor for nonlinear polarization at the ENZ frequency, (ii) SHG absorption, and (iii) fulfillment of the type-I SHG phase-matching condition corresponding to the *ooe* synchronism in the HMM shown by white curve in Fig. 3(b).

Relatively broad spectral widths of the SHG maxima for both linear polarizations of the pump beam are due to the small HMM optical thickness, which does not exceed six vacuum wavelengths near the resonance and thus masks the phase-matched SHG. To demonstrate this, we plotted the calculated relations between the fundamental wavelength (λ) and the angle of incidence (θ) when the coherent length is equal to the HMM's geometrical thickness L_{HMM}, $L_{\mathrm{HMM}} = L_c \equiv \pi/(2q_z(\lambda,\theta) - q_z(\lambda/2,\theta))$ [grey curves in Figs. 3(a) and 3(b)]; here $q_z(\lambda,\theta)$ is the spectral-angular dependence of the propagation constant in the HMM. One can see that the SHG maxima are bounded well by these curves, which supports the above statements.

Analyzing the experimental and simulations results we assert that the experimentally revealed SHG enhancement on the left edge of the laser operation range at $\theta = 20°$–$30°$ [Fig. 2(a)] and numerically obtained SHG maximum at $\lambda = 700$ nm and $\theta = 20°$–$50°$ [Fig. 3(c)] can be explained as the result of the interplay of four contributions, which specify the shape of the SHG maxima in λ-θ map: (i) phase-matching conditions fulfillment, (ii) decrease in the transmission of the TM fundamental beam near the ENZ wavelength and at increasing angle of incidence [see Figs. 1(c) and 1(d), long-wavelength regions], (iii) resonant SHG losses near the ENP wavelength [Figs. 1(c) and 1(d)], (iv) almost singular growth of the normal to the interface component of the electric field within the HMM structure at oblique incidence of the *p*-polarized light close to the ENZ wavelength.

The second peak observed on the long-wavelength edge of the laser operation range centered at $\theta = 25°$–$30°$ [Fig. 2(a)] and numerically obtained SHG peak at $\theta = 55°$–$60°$, $\lambda = 820$–840 nm [Fig. 3(a)] are also the result of the same factors except of (iv), which is significant near the ENZ wavelength.

As seen there is a qualitative agreement of the experimental and numerical results in the number of the SHG maxima and their relative intensity (Figs. 2 and 3), which justifies our statement on the phase-matching as the main mechanism

of the observed SHG spectral enhancement. Indeed, the *s*-polarized fundamental radiation gives a single SHG maximum in the long-wavelength part of the experimentally accessible spectral range [Figs. 2(b) and 3(d)], whereas in the case of *p* polarization two maxima appear at inclined incidence at short- and long-wavelength edges of the considered spectra [Figs. 2(a) and 3(c)]. In the experiment and simulations, these maxima are separated by the wavelength region with reduced SH intensity, which corresponds to the two-photon resonance of the ENP point of the HMM. We suppose that larger spectral width of the SHG intensity peaks observed in the experiment as compared to the calculated ones is the result of the dispersion of the nanorods' lengths, which can shift the HMM resonances and that was not taken into account in the modeling. As well, numerical and experimental results are in agreement with each other, demonstrating higher SH intensity when the *p*-polarized radiation illuminates the HMM as compared to the case of the *s*-polarized one [compare Figs. 2(a), 2(b) and Figs. 3(c), 3(d)].

Summing up, we have demonstrated a strong increase in the second harmonic generation in hyperbolic metamaterials composed of ordered arrays of silver nanorods in anodic aluminum oxide. The performed experiments along with the numerical modeling confirmed that this effect originates from the fulfillment of the phase-matching conditions for the SHG process. We have shown the crucial role of the two specific spectral points, ENZ and ENP, which govern the dispersion of the composite metamaterial at the SHG and fundamental wavelengths. Different types of synchronism contribute to the SHG effect for different polarizations of the fundamental laser beam, which opens a path for the phase-matched second harmonic generation in submicrometer-thick slab of nanocomposites. As well giant SHG enhancement is predicted when the second harmonic wavelength corresponds to the ENZ spectral point; in that case an increase in the Purcell factor plays a role thus making the hyperbolic metamaterias a fertile platform for the frequency conversion.

The experimental part of the work is supported by Russian Science Foundation (RSF) Grant No. 18-73-10151. Numerical calculations performed by V.B.N. are supported by RSF Grant No. 19-72-00118.

APPENDIX

Arrays of silver nanorods were prepared by templated electrodeposition of Ag using a 50-μm-thick porous anodic aluminum oxide (AAO) film as a template. The AAO template was obtained by aluminum (99.99%) anodization in 0.3 M selenic acid at 48 V and electrolyte temperature of 0 °C. After anodization, the remained aluminum was selectively dissolved in a mixture of Br_2 and CH_3OH (volume ratio of 10:90). Then, a barrier layer at the pore bases was chemically etched away in 3 M H_3PO_4 with electrochemical detection of a pore opening moment [35]. Finally, a current collector made of a 240-nm-thick Au layer was deposited onto the bottom side of the template using magnetron sputtering. The electrodeposition of silver was carried out using commercial electrolyte 07-SG (Ecomet, Russia) containing buffered $[Ag(CN)_2]^-$ (pH 9). Ag nanorods were formed at a constant potential of −0.5 V versus saturated Ag/AgCl reference electrode. Before the optical and scanning electron microscopy (SEM) measurements, the Au layer was etched away in Ar plasma. Figure 1(a) shows the SEM image of the bottom side of the obtained nanocomposite.

[1] P. Huo, S. Zhang, Y. Liang, Y. Lu, and T. Xu, Adv. Opt. Mater. **7**, 1801616 (2019).
[2] Z. Guo, H. Jiang, and H. Chen, J. Appl. Phys. **127**, 071101 (2020).
[3] M. G. Silveirinha, Phys. Rev. E **73**, 046612 (2006).
[4] N. M. Litchinitser and V. M. Shalaev, Laser Phys. Lett. **5**, 411 (2008).
[5] V. P. Drachev, W. Cai, U. Chettiar, H.-K. Yuan, A. K. Sarychev, A. V. Kildishev, G. Klimeck, and V. M. Shalaev, Laser Phys. Lett. **3**, 49 (2006).
[6] A. Poddubny, I. Iorsh, P. Belov, and Y. Kivshar, Nat. Photon. **7**, 948 (2013).
[7] P. Shekhar, J. Atkinson, and Z. Jacob, Nano Converg. **1**, 14 (2014).
[8] L. Ferrari, J. Stephen, T. Smalley, Y. Fainman, and Z. Liu, Nanoscale **9**, 9034 (2017).
[9] P. Ginzburg, F. J. R. F. no, G. A. Wurtz, W. Dickson, A. Murphy, F. Morgan, R. J. Pollard, I. Iorsh, A. Atrashchenko, P. A. Belov, Y. S. Kivshar, A. Nevet, G. Ankonina, M. Orenstein, and A. V. Zayats, Opt. Express **21**, 14907 (2013).
[10] I. A. Kolmychek, A. R. Pomozov, V. B. Novikov, A. P. Leontiev, K. S. Napolskii, and T. V. Murzina, Opt. Express **27**, 32069 (2019).
[11] X. Ni, G. V. Naik, A. V. Kildishev, Y. Barnakov, A. Boltasseva, and V. M. Shalaev, Appl. Phys. B **103**, 553 (2011).
[12] N. Vasilantonakis, M. E. Nasir, W. Dickson, G. A. Wurtz, and A. V. Zayats, Laser Photon. Rev. **9**, 345 (2015).
[13] A. V. Kabashin, P. Evans, S. Pastkovsky, W. Hendren, G. A. Wurtz, R. Atkinson, R. Pollard, V. A. Podolskiy, and A. V. Zayats, Nat. Mater. **8**, 867 (2009).
[14] O. Reshef, I. de Leon, M. Z. Alam, and R. W. Boyd, Nat. Rev. Mater. **4**, 535 (2019).
[15] G. Marino and A. Zayats, Proc. SPIE **11284**, 112840X (2020).
[16] X. Wen, G. Li, C. Gu, J. Zhao, S. Wang, C. Jiang, S. Palomba, C. M. de Sterke, and Q. Xiong, ACS Photon. **5**, 2087 (2018).
[17] A. Capretti, Y. Wang, N. Engheta, and L. D. Negro, ACS Photon. **2**, 1584 (2015).
[18] I. A. Kolmychek, V. B. Novikov, I. V. Malysheva, A. P. Leontiev, K. S. Napolskii, and T. V. Murzina, Opt. Lett. **45**, 1866 (2020).
[19] M. A. Vincenti, D. de Ceglia, A. Ciattoni, and M. Scalora, Phys. Rev. A **84**, 063826 (2011).
[20] M. A. Vincenti, D. de Ceglia, and M. Scalora, Opt. Express **28**, 31180 (2020).
[21] L. Caspani, R. P. M. Kaipurath, M. Clerici, M. Ferrera, T. Roger, J. Kim, N. Kinsey, M. Pietrzyk, A. DiFalco, V. M.

Shalaev, A. Boltasseva, and D. Faccio, Phys. Rev. Lett. **116**, 233901 (2016).
[22] L. Rodrguez-Sun, M. Scalora, A. S. Johnson, C. Cojocaru, N. Akozbek, Z. J. Coppens, D. Perez-Salinas, S. Wall, and J. Trull, APL Photon. **5**, 010801 (2020).
[23] A. P. Leontiev, O. Y. Volkova, I. A. Kolmychek, A. V. Venets, A. P. Pomozov, V. S. Stolyarov, T. V. Murzina, and K. S. Napolskii, Nanomaterials **9**, 739 (2019).
[24] Y. Sun, Z. Zheng, J. Cheng, G. Sun, and G. Qiao, Opt. Express **23**, 6370 (2015).
[25] S. Wicharn, S. Plaipichita, T. Seesanb, and P. Buranasiri, Proc. SPIE **10516**, 105161M (2018).
[26] P. Buranasiri, R. Nuansri, and S. Wicharn, Proc. SPIE **10343**, 103432W (2017).
[27] I. A. Kolmychek, A. R. Pomozov, A. P. Leontiev, K. S. Napolskii, and T. V. Murzina, Opt. Lett. **43**, 3917 (2018).
[28] R. Atkinson, W. R. Hendren, G. A. Wurtz, W. Dickson, A. V. Zayats, P. Evans, and R. J. Pollard, Phys. Rev. B **73**, 235402 (2006).
[29] S. Babar and J. H. Weaver, Appl. Opt. **54**, 477 (2015).
[30] I. H. Malitson, J. Opt. Soc. Am. **52**, 1377 (1962).
[31] P. Guyot-Sionnest, W. Chen, and Y. R. Shen, Phys. Rev. B **33**, 8254 (1986).
[32] E. A. Mamonov, T. V. Murzina, I. A. Kolmychek, A. I. Maydykovsky, V. K. Valev, A. V. Silhanek, E. Ponizovskaya, A. Bratkovsky, T. Verbiest, V. V. Moshchalkov, and O. A. Aktsipetrov, Opt. Lett. **36**, 3681 (2011).
[33] M. Kamandi, C. Guclu, T. S. Luk, G. T. Wang, and F. Capolino, Phys. Rev. B **95**, 161105(R) (2017).
[34] K. M. Schulz, D. Jalas, A. Y. Petrov, and M. Eich, Opt. Express **26**, 19247 (2018).
[35] M. Lillo and D. Losic, J. Membr. Sci. **327**, 11 (2009).